

OPEN

Lattice disorder effect on magnetic ordering of iron arsenides

Athena S. Sefat^{1*}, Xiaoping P. Wang², Yaohua Liu², Qiang Zou³, Mimgming Fu³, Zheng Gai³, Kalaiselvan Ganesan⁴, Yogesh Vohra⁴, Li Li¹ & David S. Parker¹

This study investigates magnetic ordering temperature in nano- and mesoscale structural features in an iron arsenide. Although magnetic ground states in quantum materials can be theoretically predicted from known crystal structures and chemical compositions, the ordering temperature is harder to pinpoint due to potential local lattice variations that calculations may not account for. In this work we find surprisingly that a locally disordered material can exhibit a significantly larger Néel temperature (T_N) than an ordered material of precisely the same chemical stoichiometry. Here, a EuFe_2As_2 crystal, which is a '122' parent of iron arsenide superconductors, is found through synthesis to have ordering below $T_N = 195\text{ K}$ (for the locally disordered crystal) or $T_N = 175\text{ K}$ (for the ordered crystal). In the higher T_N crystals, there are shorter planar Fe-Fe bonds [$2.7692(2)\text{ \AA}$ vs. $2.7745(3)\text{ \AA}$], a randomized in-plane defect structure, and diffuse scattering along the $[00L]$ crystallographic direction that manifests as a rather broad specific heat peak. For the lower T_N crystals, the a -lattice parameter is larger and the in-plane microscopic structure shows defect ordering along the antiphase boundaries, giving a larger T_N and a higher superconducting temperature (T_c) upon the application of pressure. First-principles calculations find a strong interaction between c -axis strain and interlayer magnetic coupling, but little impact of planar strain on the magnetic order. Neutron single-crystal diffraction shows that the low-temperature magnetic phase transition due to localized Eu moments is not lattice or disorder sensitive, unlike the higher-temperature Fe sublattice ordering. This study demonstrates a higher magnetic ordering point arising from local disorder in 122.

A bulk magnetic transition in a quantum material is thermally-driven by spin interactions dictated by nano- and mesoscale structures, such as lattice composition, crystal structure, disorder and defects, lattice strain, chemical impurities and dopants. The parents of the iron-based superconductors with $A\text{Fe}_2\text{As}_2$ ($A = \text{Ba, Sr, Ca, Eu}$) formula, known as '122', are semi-metallic with all five Fe $3d$ -bands crossing the Fermi level¹. These materials have a tetragonal structure at room temperature ($a = b \neq c$), and at a Néel antiferromagnetic transition temperature (T_N) there is a small tetragonal-to-orthorhombic structural distortion (T_s) where the unit cell rotates by $\sim 45^\circ$ within the ab -plane^{2,3}. Below T_N there is a sinusoidal modulation of Fe moments in the form of a spin-density wave (SDW)³ described by a wave vector $\mathbf{q} = (\frac{1}{2} \frac{1}{2} 1)$ in the tetragonal structure, matching the nesting vector between the electron and hole pockets at the Fermi surface⁴. The Fe spin lattice is a 'stripe' arrangement (spins are antiparallel along a - and c -axes, and parallel along b -axis)⁵⁻⁸.

It has been found that strain can induce a nematic phase transition in 122⁹ that is seen as an electronic in-plane anisotropy¹⁰, driven by orbital (unequal occupation of d_{xz} and d_{yz}) or spin directional order (not long range) that causes breaking of the in-plane C_4 rotational symmetry and splits the T_N and T_s transitions. Moreover, higher T_N in BaFe_2As_2 is linked to a more homogenous electronic structure¹¹⁻¹⁴, and there are local structure variations³. Thermally annealing of BaFe_2As_2 is found to shift and sharpen the heat capacity anomaly¹⁵. With disorder via electron irradiation in $\text{BaFe}_2(\text{As}_{1-x}\text{P}_x)_2$ the magneto-structural transition is suppressed and the superconducting dome tracks the shift of the antiferromagnetic phase¹⁶, while in $\text{Ba}_{1-x}\text{K}_x\text{Fe}_2\text{As}_2$ the antiferromagnetic and superconducting transition temperatures decrease¹⁷. For SrFe_2As_2 , in addition to a large variability of T_N values (195 to 220 K)^{6,13,18}, superconducting signature (filamentary $T_c = 21\text{ K}$) can be found in strained crystals¹⁹. Furthermore, CaFe_2As_2 can be synthesized as entirely non-magnetic, or an antiferromagnet with a large T_N , achieved by staggered alleviation of local Fe–As bonds with thermal annealing^{13,20,21}. For this study,

¹Materials Science & Technology Division, Oak Ridge National Laboratory, Oak Ridge, TN, 37831, USA. ²Neutron Scattering Division, Oak Ridge National Laboratory, Oak Ridge, TN, 37831, USA. ³Center for Nanophase Materials Sciences, Oak Ridge National Laboratory, Oak Ridge, TN, 37831, USA. ⁴Department of Physics, University of Alabama at Birmingham, Birmingham, AL, 35294, USA. *email: sefata@ornl.gov

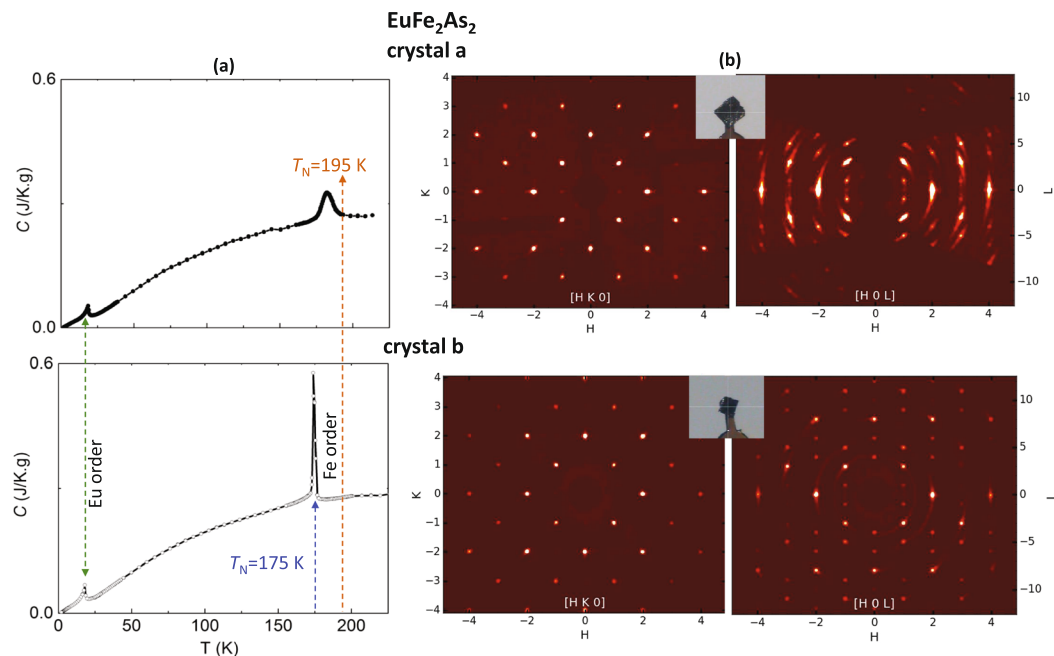


Figure 1. Data on EuFe_2As_2 ‘crystal a’ and ‘crystal b’. **(a)** Specific heat, $C(T)$, results with transitions associated with Eu ($T_N = 21$ K) and Fe ordering ($T_N = 195$ K or 175 K). **(b)** Precession images showing the $[HK0]$ and $[H0L]$ reciprocal lattice planes reconstructed from single crystal X-ray diffraction patterns measured at room temperature. Smearing in diffraction spots are more prevalent in ‘crystal a,’ noted in $[H0L]$ plane.

we hypothesize that the local lattice details, including disorder, of EuFe_2As_2 may affect its T_N value. EuFe_2As_2 is unique among the 122s for having both SDW order of Fe, and Eu local moment order below ~ 20 K with $\mathbf{q} = (0\ 0\ L)^{22-25}$. The Eu local moments are weakly coupled to the Fe sublattice and are strong enough for a large and indirect spin-lattice coupling that can lead to a structural detwinning by a small magnetic field²⁶ and can cause re-entrant non-bulk superconductivity^{27,28}.

We have synthesized two stoichiometric EuFe_2As_2 crystals with onset of Fe ordering at $T_N = 195$ K or $T_N = 175$ K, and use X-ray and neutron diffraction, microscopy and spectroscopy techniques, and theory, to understand the reasons that give these magnetic ordering temperatures. Surprisingly, the higher T_N crystal has a broader (usually associated with strain and disorder) specific heat peak, while the lower T_N crystal has a sharp peak. How does T_N relate to lattice and topological features, and does T_N value correlate with averaged lattice parameters? Would higher T_N mean more homogeneous electronic structure? What are the pressure results for diminishing antiferromagnetism and potentially deriving superconductivity in each of these crystals? Our results show that although $T_{N(\text{Fe})}$ and T_c values are greatly sensitive to the lattice details and local arrangements of defect structures, Eu ordering is unaffected at $T_{N(\text{Eu})} \approx 20$ K. This study demonstrates the apparent contradictory result that certain types of disorder can significantly increase the magnetic order, even in stoichiometric quantum material.

Experimental Procedure and Results

Single crystals of EuFe_2As_2 were grown out of a mixture of Eu and FeAs excess used as liquid flux^{12,29,30}. Each of these mixtures was warmed to 1180°C , then cooled ($2^\circ\text{C}/\text{h}$) followed by a decanting of the FeAs excess flux at 1090°C . Two different reaction loading ratios were used to obtain EuFe_2As_2 single crystals with different T_N . A loading ratio of Eu:FeAs = 1:5 gives an onset transition temperature of $T_N = 195$ K (referred to as ‘crystal a’), while Eu:FeAs = 1:4 gives crystals with $T_N = 175$ K (‘crystal b’). The chemical composition of these crystals was measured with a Hitachi S3400 scanning electron microscope operating at 20 kV. Three spots (each $\sim 80\ \mu\text{m}$ area) were checked and averaged on each crystal; energy-dispersive X-ray spectroscopy (EDS) and site-refinement of single-crystal X-ray diffraction analyses indicate that both crystals are stoichiometric and are EuFe_2As_2 . The phase purity of the crystals was checked by collecting data on an X’Pert PRO MPD X-ray powder diffractometer; structures were solely identified as tetragonal ThCr_2Si_2 structure type ($I4/mmm$, $Z = 2$).

Specific heat data were collected on EuFe_2As_2 single crystals, using a Quantum Design Physical Property Measurement System (PPMS); the $C(T)$ results are shown in Fig. 1a. Each EuFe_2As_2 crystal exhibits two transitions: an ordering of the Fe lattice at higher temperature, followed by lower temperature ordering (≈ 20 K) due to Eu moments. The EuFe_2As_2 ‘crystal a’ exhibits the higher onset ordering temperature of $T_N = 195$ K with a broader peak, compared to ‘crystal b’ giving a sharp lambda transition below $T_N = 175$ K. The specific heat result of ‘crystal a’ looks similar to that reported in a pressed polycrystalline sample (with respect to peak width, height, and transition temperature)²².

To analyze crystal structures, single crystal X-ray diffraction data were collected at room temperature on a Rigaku XtaLAB PRO diffractometer (Mo Source, $K_\alpha = 0.71073\ \text{\AA}$) equipped with a DECTRIS Pilatus 200 K area

EuFe ₂ As ₂ sample ID	'crystal a'	'crystal b'
<i>a</i> (Å)	3.9162 (3)	3.9238 (4)
<i>c</i> (Å)	12.104 (3)	12.105 (2)
As at (0, 0, <i>z</i>); 4e		
<i>z</i>	0.36256 (13)	0.36255 (11)
<i>U</i> _{iso}	0.0104 (6)	0.0109 (6)
arsenic height, Å	1.3624 (10)	1.3624 (8)
site occupancy	0.96 (9)	0.97 (8)
Fe at (½, 0, ¼); 4d		
<i>U</i> _{iso}	0.0106 (6)	0.0107 (6)
Fe–Fe distance, Å	2.7692 (2)	2.7745 (3)
site occupancy	0.97 (9)	0.97 (8)

Table 1. Single-crystal X-ray diffraction refinement on the two crystals of EuFe₂As₂: 'crystal a' ($T_N = 195$ K), 'crystal b' ($T_N = 175$ K).

detector. Data collection and reduction used the CrysAlisPro program³¹. Crystal structure refinements were performed using the SHELX-2014 program³². Figure 1b (insets) shows the pictures of crystals for the data collection, stuck on top of needles. Crystals 'a' and 'b' appeared similar visually, with sheet morphologies; [001] direction is perpendicular to the plane of the plate. Figure 1b gives the precession images of [HK0] and [H0L] reciprocal lattice planes, showing lattice strain effects associated with smeared diffraction spots in the L direction for 'crystal a'; this crystal has a relatively broad C(T) peak ($T_N = 195$ K) from the Fe ordering. A broader peak of specific heat is usually associated with lattice strain and disorder. Table 1 shows the lattice parameters and refinement results of the X-ray structure measured at room temperature. The EuFe₂As₂ sample with higher T_N ('crystal a') gives a lower overall *a*-lattice parameter and a shorter planar Fe–Fe distance of 2.7692(2) Å, indicating a contraction of 0.0053(4) Å for the in-plane Fe–Fe bond when compared to that of 2.7745(3) Å for the lower T_N ('crystal b').

Neutron diffraction measurements were carried out using the TOPAZ single crystal diffractometer at the ORNL Spallation Neutron Source (SNS), which uses the wavelength-resolved Laue technique with an extensive array of neutron time-of-flight area detectors for 3-dimensional Q space mapping of Bragg and diffuse scattering patterns originating from magnetic and nuclear phase transitions³³. Pieces of 'crystal a' and 'crystal b' had dimensions of 3.25 × 2.50 × 0.20 mm³ and 2.75 × 2.63 × 0.30 mm³, respectively, and were attached on a MiTegen loop using super glue for data collection at room temperature and 95 K. Each of the samples was oriented with high precision for volumetric sampling of Bragg peaks in specific directions with the CrystalPlan program^{34,35}. At room temperature, the (0 2 0)_{Tetragonal} peak profiles for the two EuFe₂As₂ crystals are shown in Fig. 2, demonstrating the peak false-color maps and their corresponding peak intensity profiles along the crystallographic *c*-direction. The peak from 'crystal a' is broad and shows extensive diffuse lines along the L direction, which is consistent with that observed in X-ray diffraction, and gives broader and higher T_N in C(T).

As shown in Fig. 1b, the streaks for the (2 0 0) peak along L direction for 'crystal a' is much more pronounced (Fig. 2a) than that of 'crystal b' (Fig. 2b), which could be induced by strain, stacking fault or disorder in the bulk single crystal sample. Since the refined average *c* lattice parameter remains essentially unchanged for both crystals (Table 1), the much more pronounced streaks for 'crystal a' are likely from microstrain caused by randomly distributed defects in 'crystal a', which is evident from scanning tunneling microscopy/spectroscopy (STM/S) measurement (see Fig. 3 below). The split of the peaks along *c* also indicates twinning and multidomain structures of 'crystal a'. In particular, we note from Fig. 2 (bottom panels) that the full-width at half maximum (FWHM) for the (2 0 0) peak along L direction is some 0.13–0.27 reciprocal lattice units larger than that of 'crystal b'. If one assumes that in the ordered 'crystal b' the finite (i.e. non-zero) FWHM is largely due to measurement resolution limits, the FWHM for 'crystal a' would correspond to a ~2–5% local variation in the lattice constant *c*.

For these crystals, neutron diffraction results were additionally carried out at 95 K, to confirm the Fe magnetic peak below T_N in accordance with the propagation vector $\mathbf{q} = (1\ 0\ 1)_{\text{Orthorhombic}} = (\frac{1}{2}\ \frac{1}{2}\ 1)_{\text{Tetragonal}}$ and the stripe arrangement of the Fe spin lattice^{5–8} (see Fig. S1a in Supplementary). Additionally, variable temperature scans of the Eu magnetic peak at (0 3 0) for both crystals were performed below 30 K using the elastic diffuse scattering spectrometer CORELLI at SNS³² and showed the same temperature dependence of Eu magnetic peak as (0 3 0) with $T_N = 21$ K (see Fig. S1b). In contrast, the Néel transition temperature for Fe is clearly lattice and disorder sensitive. The high-temperature phase transition is due to the ordering of the transition metal Fe moments, whereas the low-temperature phase transition is due to the ordering of the localized Eu moments²². The divergent behavior of the Fe and Eu sublattices from 'crystal a' to 'b' – the former sublattice sensitive to lattice disorder, the latter insensitive – is of interest here. One plausible hypothesis is that the Eu 4*f* moments are much more localized, near the Eu nucleus, than the Fe moments that are more itinerant. This would suggest that the Eu 4*f* moments are less subject to nano-strain than the Fe 3*d* moments, and the relatively isolated location of Eu between the layers (as opposed to the tightly bound FeAs layers) would enhance this possibility. Supporting this assertion is the relative insensitivity of Eu ordering temperature to pressure (see Fig. S4), again unlike the Fe sublattice ordering. Indeed the Eu magnetic order survives to higher pressure than the Fe order, despite occurring at much lower temperatures.

To further investigate the local origin of the bulk T_N differences between the two EuFe₂As₂ crystals, surface topography and electronic structures were investigated using STM/S on *in-situ* low-temperature cleaved surfaces.

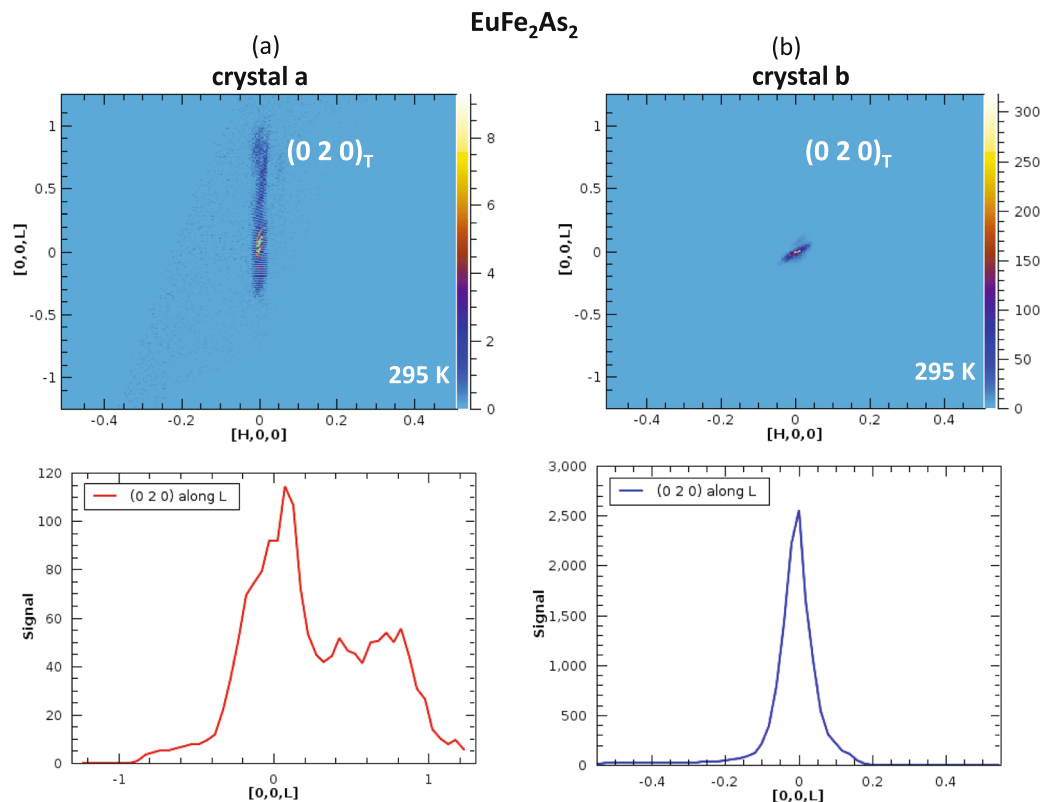


Figure 2. Tetragonal (0 2 0) peak profiles for the two EuFe_2As_2 crystals at room temperature for (a) ‘crystal a’ and (b) ‘crystal b’, showing the peak false color maps, and their corresponding peak intensity profiles along the crystallographic c direction. Note the difference in scales on both axes. The peak from ‘crystal a’ is substantially broadened showing extended diffuse lines.

The two sets of EuFe_2As_2 ‘crystal a’ and ‘crystal b’ were cleaved in an ultra-high vacuum at ~ 78 K and then immediately transferred to the STM/S head precooled to 4.2 K without breaking vacuum. The STM/S experiments were carried out using a scanning tunneling microscope with base pressure better than 2×10^{-10} Torr, with mechanically cut Pt-Ir tip. All Pt-Ir tips were conditioned on clean Au (1 1 1) and checked using the topography, surface state, and work function before each measurement. The STM/S were controlled by the SPECS Nanonis control system. Topographic images were acquired in constant current mode with bias voltage applied to samples, and tip grounded. All the spectroscopies were obtained using the lock-in technique with a modulation of 1 mV at 973 Hz on bias voltage, dI/dV . Current-imaging-tunneling-spectroscopy were collected over a grid of pixels at bias ranges around Fermi level using the same lock-in amplifier parameters. The survey on multiple large areas of both samples shows the coexistence surface reconstructions on ‘crystal a’ and ‘crystal b’, as shown in Fig. 3. Using a similar method as STM report on Co-doped BaFe_2As_2 ³⁶, the 2×1 and $\sqrt{2} \times \sqrt{2}$ reconstructed surfaces can be assigned to arsenic termination and europium termination, respectively, as shown in Fig. 3a. While the 2×1 surfaces of both crystals (Fig. 3b,c) are very similar, the $\sqrt{2} \times \sqrt{2}$ surfaces of the two crystals (Fig. 3d,e) are very different. The atomic resolved images in the insets of Fig. 3d,e from the well-ordered $\sqrt{2} \times \sqrt{2}$ reconstructed areas of the two crystals are similar, but the arrangements of the defects on the surfaces are rather different. In ‘crystal a’, surface defects (one of the defects is marked with a black arrow in Fig. 3d) are essentially randomly distributed on the surface, but in ‘crystal b’, large amount of defects prefer to form into chains (one of the chains is marked with a white arrow in Fig. 3e). By analyzing atomically resolved images around these areas, we found the chains are aligned on the antiphase boundaries. Because the surface reconstruction is 2×1 or $\sqrt{2} \times \sqrt{2}$, those domains can shift by 1 to form antiphase boundaries. Although antiphase boundaries also exist on the ‘crystal a’ surface (one of the antiphase boundaries is marked with a green arrow in Fig. 3d), defects in ‘crystal a’ do not segregate along the boundaries. The electronic properties revealed by the STS from the surfaces are consistent with the morphological observation (see also Fig. S2). In Fig. 3f, the average electronic local density of states (LDOS) of 2×1 surfaces (As termination) over large areas are almost identical for both crystals, but the LDOS from the two $\sqrt{2} \times \sqrt{2}$ surfaces (Eu termination) in Fig. 3g have significant differences. This shows that the different arrangements of the surface defects in the two crystals change the electronic structure dramatically. Given the preparation of these surfaces by cleaving the crystals in ultra-high vacuum at low temperatures, this difference is in electronic structure that is generally reflective of the effects of the defects in the bulk crystals.

For both EuFe_2As_2 crystals, high-pressure electrical-resistance measurements were performed using a diamond anvil cell (see Figs. S3 and S4), to explore the differences of pressure effects on the two crystals that have different T_N , under the same experimental setup. Although the feature due to Eu ordering is not changed for either crystals up to ~ 4 GPa, Fe ordering is greatly sensitive to pressure and the rate of T_N suppression for both crystals is

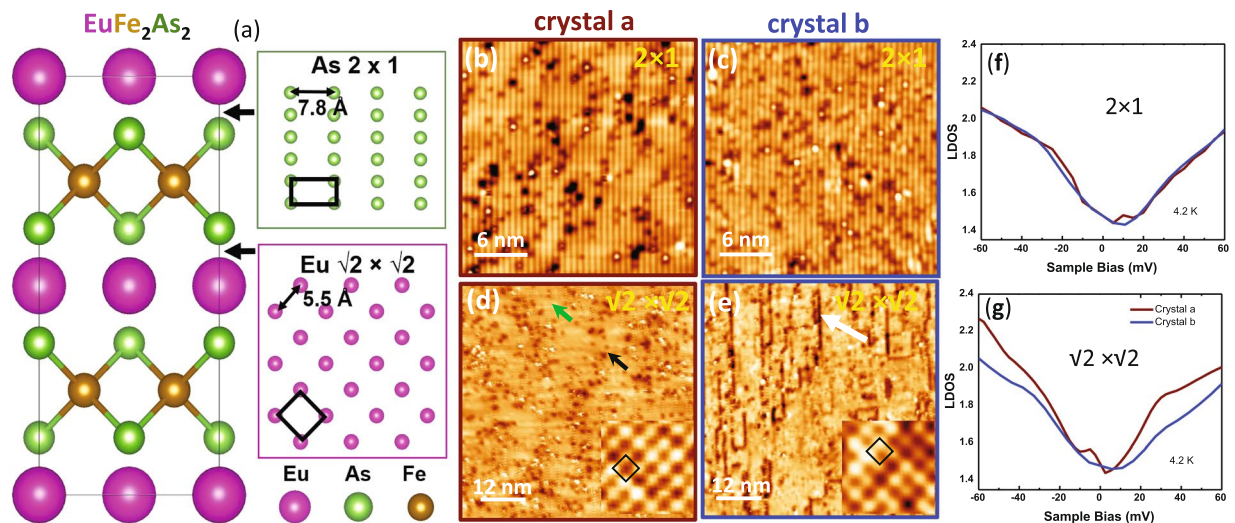


Figure 3. (a) The structure model of EuFe_2As_2 and the surface reconstruction models of arsenic 2×1 and europium $\sqrt{2} \times \sqrt{2}$ terminations. The black boxes outline the unit cells. (b,c) Topographic images of 2×1 surface reconstruction from 'crystal a' (-500 mV , 100 pA) and 'crystal b' (-1 V , 100 pA), respectively. (d,e) Topographic images of $\sqrt{2} \times \sqrt{2}$ surface reconstruction from 'crystal a' (-60 mV , 400 pA) and 'crystal b' (-20 mV , 800 pA), respectively. Insets show the atomic resolved images in $3 \times 3 \text{ nm}^2$ size and black boxes are the unit cells of $\sqrt{2} \times \sqrt{2}$ surface reconstruction. (f,g) Comparison of average LDOS from 'crystal a' (red) and 'crystal b' (blue), for surface reconstructions at 4.2 K .

similar. For 'crystal b' with smaller $T_N = 175 \text{ K}$, the drop in resistivity is noticed at lower pressure of 2.5 GPa , compared to 'crystal a', with a drop in resistivity at 3.2 GPa . EuFe_2As_2 with sharper, but lower T_N , is prone to a higher superconducting dome (S4); highest T_c value for 'crystal a' is 36 K , and for 'crystal b' is 41 K .

First Principles Calculations

In the effort to understand the sample-to-sample variation in Néel temperatures, we have conducted first principles theory calculations of the effect of nano-scale strain on the magnetic order, specifically on two questions. The first question is straightforward: is the observed variation in T_N related to the slight difference in planar lattice constants in crystals 'a' and 'b'? We assess based on calculations of the 'ordering energy', specifically the difference in energy between the stripe ground-state and the checkerboard (all neighboring moments are anti-aligned) excited state. The second question, with more complex interpretation, is whether c -axis strain is relevant to the observed T_N variation. The motivation for studying this question is the evident 'shoulder' in the neutron diffraction results presented in Fig. 2a, which could result from c -axis nano-scale strain, and thereby an effective distribution of local c -axis lattice parameters. Note that the bulk lattice constants for crystals 'a' and 'b' are identical (to within 0.001 \AA), so that we are studying, in effect, the local nanoscale energetics rather than constructing an involved model of the bulk Néel point variation for a sample with a distribution of local lattice constants.

First principles calculations were performed using the linearized augmented plane wave (LAPW) density functional theory code WIEN2K³⁷. As in our previous work¹⁴ we have used the local density approximation (LDA), with arsenic height and lattice parameters taken directly from our experimental XRD refinements (Table 1), except as stated below. An RK_{max} value of 8.0 – the product of the smallest sphere radius and largest plane-wave expansion wavevector – was used. To avoid the generally confounding complexities of $4f$ physics (here we are focused on the Fe magnetic behavior) we have followed our previous theoretical work³⁸ and performed the all-electron calculations with the isoelectronic substitution of Sr for the divalent Eu, but retained our lattice parameters and internal coordinates for EuFe_2As_2 . The effect of these choices is to allow a direct evaluation of the Fe sublattice magnetic properties without the need to apply a correlated (i.e. LDA + U) approach to deal with the Eu $4f$ electrons, which play little or no role in the Fe magnetism. Sphere radii of 2.5 Bohr were used for Sr, and between 2.26 and 2.30 for Fe (depending on volume), and between 2.15 and 2.22 for As. Identical sphere radii were used for the calculations at given volume, relevant for assessing the interlayer coupling.

With regards to the first question of whether changes in the magnetic ordering energy, or energetic difference between the stripe ground state and checkerboard excited state, result from the small difference in planar lattice parameters, we find only a small change (0.4%) in this energy, from 51.6 meV/Fe for 'crystal a', to 51.8 meV/Fe for 'crystal b'. This means that the observed $\sim 10\%$ Néel temperature variation does not result from changes in this ordering energy. At the same time, one should note that the observed 0.2% change in lattice parameter from 'crystal a' to 'b' corresponds to an effective chemical pressure of several tenths of a GPa, and pressure is a well-known means of T_N suppression. While it remains possible that this effective planar strain is relevant here, arguing against this is the fact that the smaller lattice parameter 'crystal a' has the larger Néel point, whereas the application of pressure, thereby yielding smaller lattice constants, generally lowers the T_N .

Concerning the second question, the neutron scan of ‘crystal a’ along the [00 L] direction shows clear evidence of disorder, with a rather broadened peak around the (0 0 0) point and a substantial ‘shoulder’ feature extending nearly to the [001] point (Fig. 2a). While there are many possible sources of such disorder, ranging from vacancies and anti-site defects to small grain sizes, here we explore the idea that *c*-axis strain in ‘crystal a’ is ultimately responsible for the rather broad neutron diffraction peaks. The hypothesis here is that nanoscale *c*-axis strain could significantly change the interlayer magnetic coupling, since this coupling is known from previous work³⁹ to depend rather substantially on pressure, or equivalently compression or expansion of the cell from the equilibrium value. The interlayer coupling is of course necessary to attain a finite ordering temperature, given the Mermin-Wagner finding that truly low-dimensional systems do not order at finite temperature. Since, as in many materials, the interlayer coupling here is relatively weak, it is plausible that nanoscale *c*-axis strain could change the coupling, which generally falls off quickly with increased distance.

We have therefore conducted calculations of this interlayer magnetic coupling. Here we report the energy difference, per unit cell, between the ground-state stripe magnetic order (which is antiferromagnetically coupled along the *c*-axis) and a state with ferromagnetic *c*-axis coupling. We have done this at the experimental lattice parameter of 12.104 Å, and in addition for *c* values 5% larger and smaller than this value. For the experimental *c*-lattice parameter, we find an interlayer coupling energy difference of 7.1 mRyd/u.c., which increases slightly to 7.7 mRyd for the +5% *c* value, but decreases sharply to some 4.5 mRyd for the –5% *c* value. These values are in qualitative agreement with the previous work on BaFe₂As₂³⁹, where it was found that the application of pressure decreases the interlayer coupling. We mention also that the calculated magnetic moments decrease substantially for the smaller cell, and correspondingly increase for the larger cell. In the antiferromagnetically coupled layer state, for the smallest cell these moments are 1.25 μ_B per Fe, for the experimental cell the value is 1.63 μ_B, and for the largest cell is 1.92 μ_B. Neutron diffraction results give an Fe moment of ~1 μ_B⁸, consistent with the general overstatement of magnetic order by first principles approaches in these materials.

These data suggest that interlayer strain can affect the magnetism in a substantial manner. In this scenario, the broadened specific heat peak in ‘crystal a’ would result from a *distribution* of local lattice parameters, and thereby a distribution of local interlayer exchange couplings, resulting in a spread of ordering points. However, one difficulty with this argument is that such a distribution would have a larger effect on the temperature width of the transition than the mean transition temperature, since the bulk *c*-axis lattice parameters in crystals ‘a’ and ‘b’ are identical (leaving aside such questions as the temperature dependence of the magnetic correlation length in such a disordered scenario). Furthermore the fact that the strained calculations show larger *decreases* in magnetic order (measured as the interlayer coupling) with compressive strain than *increases* with tensile strain suggests that the effect of a distribution of *c*-axis lattice parameters around the bulk value would be a *decrease* in Néel point, not an increase. If the reverse were true – that the increases in magnetic order with one form of strain were larger than the decreases with the opposite strain – one would in fact have a possible explanation for the *T_N* enhancement. However, the calculations do not suggest this latter possibility, and thus we must consider, as unsupported the hypothesis, that strain-related interlayer-magnetic exchange differences create the observed *T_N* increase in ‘crystal a’.

Since the straightforward explanations of the *T_N* increase, based on disorder-induced structure modification, do not explain this rather unusual behavior, it is necessary to consider other possibilities. For example, in materials near a magnetic instability, it has recently been posited⁴⁰ that charge doping can induce a magnetic transition based on Stoner physics, and one could plausibly imagine a similar enhancement in magnetic character of an already magnetic material. However, the generally stoichiometric character of both samples studied here argues against such a possibility. An additional possibility is provided by the theoretical work of Gastiasoro *et al.*⁴¹, which finds (for superconductivity, and extended to magnetic order) density-of-states increase from either resonant states or Anderson localization leading to enhancements in ordering points. We here suggest a different possibility: spin fluctuations are known to be exceptionally strong in the iron arsenides, and in fact are a leading candidate for the interaction causing superconductivity. It is commonly believed⁴² that these fluctuations also play an important role in reducing the Néel point of these materials from a much higher ‘bare’ value. It is also known from several recent theory works^{43,44} that disorder can play a substantial role in weakening spin fluctuations and inducing magnetism, and this role is especially prominent⁴⁵ in the case of stripe magnetic order, as is observed in the iron-arsenides. Putting such arguments together, we suggest that the disorder evident in our specific heat and neutron data is weakening the spin fluctuations and thereby enhancing the magnetic order.

One means of testing this theory would be to employ the quasi-particle interference techniques recently applied to LiFeAs⁴⁶. While in that work it was the superconductivity (and its coupling to a bosonic excitation) that was studied, we anticipate that a measure suitably adapted to the case of the antiferromagnetic order here could also yield insight. If reduced spin fluctuations are in fact at work here, the momentum and energy dependent differential conductance *g*(**k**, ω) should show signatures of reduced scattering in the higher *T_N*. In particular, generally sharper (as a function of momentum and energy) peaks are expected in the conductance in this material, when measured at the same temperature as the lower Néel point crystal. Future experimental studies would be highly beneficial are to assess this possibility.

Conclusion

We find that disorder-related lattice variability drives significantly different Fe Néel ordering temperatures in the stoichiometric EuFe₂As₂ crystals, with the highly unusual result that the *more* locally disordered crystal exhibits the *higher* Néel point. The diffuse scattering that is seen along the [00 L] direction in X-ray and neutron diffraction measurements for the higher *T_N* crystal may well be the origin of the broadened specific heat peak and the suppressed superconducting dome. The surface topography and electronic structure studies show that there is a clear difference in electronic and defect structures between the two *T_N* crystals, with defect states dominating and elevating the LDOS for the higher *T_N* ‘crystal a’. Although the two crystals have a similar number of defects, their

segregation around the antiphase boundaries in 'crystal b' largely decreases the number of random individual defects, which may cause a higher- T_c superconductor with pressure. This study thereby demonstrates the modification of T_N in an iron arsenide by controlled disorder, thus explaining the observation of substantial ordering temperature variations for these stoichiometric quantum materials in the literature.

Received: 5 August 2019; Accepted: 4 December 2019;

Published online: 27 December 2019

References

- Sefat, A. S. & Singh, D. J. Chemistry and electronic structure of iron-based superconductors. *MRS Bull.* **36**, 614 (2011).
- Fisher, I. R., Degiorgi, L. & Shen, Z. X. In-plane electronic anisotropy of underdoped '122' Fe-arsenide superconductors revealed by measurements of detwinned single crystals. *Rep. Prog. Phys.* **74**, 124506 (2011).
- Niedziela, J. L., McGuire, M. A. & Egami, T. Local structural variation as source of magnetic moment reduction in BaFe₂As₂. *Phys. Rev. B* **86**, 174113 (2012).
- Ding, H. *et al.* Observation of Fermi-surface-dependent nodeless superconducting gaps in Ba_{0.6}K_{0.4}Fe₂As₂. *Europhys. Lett.* **83**, 47001 (2008).
- Huang, Q. *et al.* Neutron-diffraction measurements of magnetic order and a structural transition in the parent BaFe₂As₂ compound of FeAs-based high-temperature superconductors. *Phys. Rev. Lett.* **101**, 257003 (2008).
- Zhao, J. *et al.* Spin and lattice structures of single-crystalline SrFe₂As₂. *Phys. Rev. B* **78**, 140504 (2008).
- Goldman, A. I. *et al.* Lattice and magnetic instabilities in CaFe₂As₂: A single-crystal neutron diffraction study. *Phys. Rev. B* **78**, 100506 (2008).
- Xiao, Y. *et al.* Brueckel, Magnetic structure of EuFe₂As₂ determined by single-crystal neutron diffraction. *Phys. Rev. B* **80**, 174424 (2009).
- Zhang, W.-L., Sefat, A. S., Ding, H., Richard, P. & Blumberg, G. Stress-induced nematicity in Eu Fe₂As₂ studied by Raman spectroscopy. *Phys. Rev. B* **94**, 014513 (2016).
- Chu, J.-H., Kuo, H.-H., Analytis, J. G. & Fisher, I. R. Divergent nematic susceptibility in an iron arsenide superconductor. *Science* **337**, 710 (2012).
- Rotter, M. *et al.* Spin-density-wave anomaly at 140 K in the ternary iron arsenide BaFe₂As₂. *Phys. Rev. B* **78**, 020503 (2008).
- Sefat, A. S. *et al.* Superconductivity at 22 K in Co-doped BaFe₂As₂ crystals. *Phys. Rev. Lett.* **101**, 117004 (2008).
- Saparov, B. & Sefat, A. S. Annealing effects on the properties of BFe₂As₂ (B = Ca, Sr, Ba) superconducting parents. *Dalton Trans.* **43**, 14971 (2014).
- Li, L. *et al.* Improving superconductivity in BaFe₂As₂-based crystals by cobalt clustering and electronic uniformity. *Sci. Rep.* **7**, 949 (2017).
- Rotundu, C. R. *et al.* Heat capacity study of BaFe₂As₂: Effects of annealing. *Phys. Rev. B* **82**, 144525 (2010).
- Mizukami, Y. *et al.* Impact of disorder on the superconducting phase diagram in BaFe₂(As_{1-x}P_x)₂. *J. Phys. Soc. Jpn.* **86**, 083706 (2017).
- Prozorov, R. *et al.* Interplay between superconductivity and itinerant magnetism in underdoped Ba_{1-x}K_xFe₂As₂ (x = 0.2) probed by the response to controlled point-like disorder. *Quant. Mater.* **4**, 737 (2019).
- Chen, G.-F. *et al.* Superconductivity in Hole-Doped (Sr_{1-x}K_x)Fe₂As₂. *Chin. Phys. Lett.* **25**, 3403 (2008).
- Saha, S. R., Butch, N. P., Kirshenbaum, K., Paglione, J. & Zavalij, P. Y. Superconducting and ferromagnetic phases induced by lattice distortions in stoichiometric SrFe₂As₂ single crystals. *Phys. Rev. Lett.* **103**, 037005 (2009).
- Saparov, B. *et al.* Complex structures of different CaFe₂As₂ samples. *Sci. Rep.* **4**, 4120 (2014).
- Gofryk, K. *et al.* Fermi-surface reconstruction and complex phase equilibria in CaFe₂As₂. *Phys. Rev. Lett.* **112**, 186401 (2014).
- Ren, Z. *et al.* Antiferromagnetic transition in EuFe₂As₂: A possible parent compound for superconductors. *Phys. Rev. B* **78**, 052510 (2008).
- Koo, J. *et al.* Magnetic and structural phase transitions of EuFe₂As₂ studied via neutron and resonant X-ray scattering. *J. Phys. Soc. Jpn.* **79**, 114708 (2010).
- Herrero-Martín, J. *et al.* Magnetic structure of EuFe₂As₂ as determined by resonant x-ray scattering. *Phys. Rev. B* **80**, 134411 (2009).
- Jeevan, H. S. *et al.* Electrical resistivity and specific heat of single-crystalline EuFe₂As₂: A magnetic homologue of SrFe₂As₂. *Phys. Rev. B* **78**, 052502 (2008).
- Zapf, S. *et al.* Persistent detwinning of iron-pnictide EuFe₂As₂ crystals by small external magnetic fields. *Phys. Rev. Lett.* **113**, 227001 (2014).
- Park, K., Louca, D., Llobet, A. & Yan, J.-Q. Evidence of local disorder in the overdoped regime of Ba(Fe_{1-x}Cox)₂As₂. *Phys. Rev. B* **84**, 024502 (2011).
- Paramanik, U. B. *et al.* Reentrant superconductivity in Eu(Fe_{1-x}Ir_x)₂As₂. *J. Phys.: Condes. Matter* **25**, 265701 (2013).
- Saparov, B., Mitchell, J. E. & Sefat, A. S. Properties of binary transition-metal arsenides (TAs). *Supercond. Sci. Technol.* **25**, 084016 (2012).
- Sefat, A. S. Bulk synthesis of iron-based superconductors. *Curr. Opin. Solid State & Mater. Sci.* **17**, 59 (2013).
- CrysAlisPro 1.171.39.9g, Data Collection and Processing Software for Agilent X-ray Diffractometers, Rigaku Oxford Diffraction (2017).
- Sheldrick, G. M. Crystal structure refinement with SHELXL. *Acta Cryst. C* **71**, 3 (2015).
- Schultz, A. J. *et al.* Integration of neutron time-of-flight single-crystal Bragg peaks in reciprocal space. *J. Appl. Crystallogr.* **47**, 915 (2014).
- Michels-Clark, T. M., Savici, A. T., Lynch, V. E., Wang, X. P. & Hoffmann, C. M. Expanding Lorentz and spectrum corrections to large volumes of reciprocal space for single-crystal time-of-flight neutron diffraction. *J. Appl. Crystallogr.* **49**, 497 (2016).
- Ye, F., Liu, Y., Whitfield, R., Osborn, R. & Rosenkranz, S. Implementation of cross correlation for energy discrimination on the time-of-flight spectrometer CORELLI. *J. Appl. Crystallogr.* **51**, 315 (2018).
- Zou, Q. *et al.* Effect of surface morphology and magnetic impurities on the electronic structure in cobalt-doped BaFe₂As₂ superconductors. *Nano Letters* **17**, 1642 (2017).
- Blaha, P. *et al.* WIEN2k, An augmented plane wave + local orbitals program for calculating crystal properties (Karlheinz Schwarz, Techn. Universität Wien, Austria), ISBN 3-9501031-1-2 (2018).
- Moon, S. J. *et al.* Dual character of magnetism in EuFe₂As₂: Optical spectroscopic and density-functional calculation study. *Phys. Rev. B* **81**, 205114 (2010).
- Johannes, M. D., Mazin, I. I. & Parker, D. S. Effect of doping and pressure on magnetism and lattice structure of iron-based superconductors. *Phys. Rev. B* **82**, 024527 (2010).
- Pandey, T. & Parker, D. S. Borderline magnetism: How adding Mg to paramagnetic CeCo₃ makes a 450-K ferromagnet with large magnetic anisotropy. *Phys. Rev. Appl.* **10**, 034038 (2018).
- Gastiasoro, M. N. & Andersen, B. M. Enhancing superconductivity by disorder. *Phys. Rev. B* **98**, 184510 (2018).
- Ortenzi, L. *et al.* Structural Origin of the Anomalous Temperature Dependence of the Local Magnetic Moments in the CaFe₂As₂ Family of Materials. *Phys. Rev. Lett.* **114**, 047001 (2015).

43. Andersen, B. M., Graser, S. & Hirschfeld, P. J. Disorder-Induced Freezing of Dynamical Spin Fluctuation in Underdoped Cuprates. *Phys. Rev. Lett.* **105**, 147002 (2010).
44. Andersen, B. M., Hirschfeld, P. J., Kampf, A. P. & Schmid, M. Disorder-Induced Static Antiferromagnetism in Cuprate Superconductors. *Phys. Rev. Lett.* **99**, 147002 (2007).
45. Martiny, J. H. J., Kreisel, A. & Andersen, B. M. Theoretical study of impurity-induced magnetism in FeSe. *Phys. Rev. B* **99**, 014509 (2019).
46. Allan, M. P. *et al.* Identifying the ‘fingerprint’ of antiferromagnetic spin fluctuations in iron pnictide superconductors. *Nat. Phys.* **11**, 177 (2015).

Acknowledgements

The research is primarily supported by the U.S. Department of Energy (DOE), Office of Science, Basic Energy Sciences (BES), Materials Science and Engineering Division. Neutron scattering experiments at Oak Ridge National Laboratory (ORNL) were supported by the Scientific User Facilities Division, Office of BES, DOE.

Author contributions

Sefat: Measured bulk properties, wrote paper. Wang: Performed single crystal X-ray diffraction. Liu: Performed single crystal neutron diffraction. Zou, Fu, Gai: Performed STM/S. Kalaiselvan, Vohra: Performed high pressure resistivity measurements. Li: synthesized crystals. Parker: theory calculations.

Competing interests

The authors declare no competing interests.

Additional information

Supplementary information is available for this paper at <https://doi.org/10.1038/s41598-019-56301-5>.

Correspondence and requests for materials should be addressed to A.S.S.

Reprints and permissions information is available at www.nature.com/reprints.

Publisher’s note Springer Nature remains neutral with regard to jurisdictional claims in published maps and institutional affiliations.



Open Access This article is licensed under a Creative Commons Attribution 4.0 International License, which permits use, sharing, adaptation, distribution and reproduction in any medium or format, as long as you give appropriate credit to the original author(s) and the source, provide a link to the Creative Commons license, and indicate if changes were made. The images or other third party material in this article are included in the article’s Creative Commons license, unless indicated otherwise in a credit line to the material. If material is not included in the article’s Creative Commons license and your intended use is not permitted by statutory regulation or exceeds the permitted use, you will need to obtain permission directly from the copyright holder. To view a copy of this license, visit <http://creativecommons.org/licenses/by/4.0/>.

© The Author(s) 2019